Development of acoustic model-based iterative reconstruction technique for thick-concrete imaging

Hani Almansouri, Dwight Clayton, Roger Kisner, Yarom Polsky, Charles Bouman, and Hector Santos-Villalobos

Articles you may be interested in

Can conclusions drawn from phantom-based image noise assessments be generalized to in vivo studies for the nonlinear model-based iterative reconstruction method?
Med. Phys. **43**, 687 (2016); 10.1118/1.4939257

MO-FG-204-09: High Spatial Resolution and Artifact-Free CT Bone Imaging at Off-Centered Positions: An Application of Model-Based Iterative Reconstruction
Med. Phys. **42**, 3571 (2015); 10.1118/1.4925430

SU-E-I-33: Initial Evaluation of Model-Based Iterative CT Reconstruction Using Standard Image Quality Phantoms
Med. Phys. **41**, 137 (2014); 10.1118/1.4887981

Model-based microwave image reconstruction: simulations and experiments
Med. Phys. **31**, 3231 (2004); 10.1118/1.1812871

Iterative model-based automatic target recognition for acoustic landmine detection
J. Acoust. Soc. Am. **110**, 2740 (2001); 10.1121/1.4809049

Development of Acoustic Model-Based Iterative Reconstruction Technique for Thick-Concrete Imaging

Hani Almansouri[2,b)], Dwight Clayton[1,c)], Roger Kisner[1,d)], Yarom Polsky[1,e)], Charles Bouman[2,f)] and Hector Santos-Villalobos[1,a)]

[1]*Oak Ridge National Laboratory, One Bethel Valley Road, Oak Ridge, TN 37831*
[2]*Pudue University, 610 Purdue Mall, West Lafayette, IN 47907*

a)Corresponding author: hsantos@ornl.gov
b)halmanso@purdue.edu
c)claytonda@ornl.gov
d)kisnerra@ornl.gov
e)polskyy@ornl.gov
f)bouman@purdue.edu

Abstract. Ultrasound signals have been used extensively for non-destructive evaluation (NDE). However, typical reconstruction techniques, such as the synthetic aperture focusing technique (SAFT), are limited to quasi-homogenous thin media. New ultrasonic systems and reconstruction algorithms are in need for one-sided NDE of non-homogenous thick objects. An application example space is imaging of reinforced concrete structures for commercial nuclear power plants (NPPs). These structures provide important foundation, support, shielding, and containment functions. Identification and management of aging and degradation of concrete structures is fundamental to the proposed long-term operation of NPPs. Another example is geothermal and oil/gas production wells. These multi-layered structures are composed of steel, cement, and several types of soil and rocks. Ultrasound systems with greater penetration range and image quality will allow for better monitoring of the well's health and prediction of high-pressure hydraulic fracturing of the rock. These application challenges need to be addressed with an integrated imaging approach, where the application, hardware, and reconstruction software are highly integrated and optimized. Therefore, we are developing an ultrasonic system with Model-Based Iterative Reconstruction (MBIR) as the image reconstruction backbone. As the first implementation of MBIR for ultrasonic signals, this paper document the first implementation of the algorithm and show reconstruction results for synthetically generated data.[1]

INTRODUCTION

Non-Destructive Evaluation (NDE) of complex, non-homogenous, thick objects may extend the operational life of nuclear facilities, bridges, and production wells and provide better characterization of hard to access sub-surfaces. For example, all commercial nuclear power plants (NPPs) in the United States contain concrete structures. Fig. 1a shows the Chapelcross Nuclear Power Station in Scotland [1]. Typical concrete structures in these plants can be grouped into four general categories: primary containment buildings, containment internal structures, secondary containments/reactor buildings, and other structures, such as spent fuel pools and cooling towers. These structures provide important foundation, support, shielding, and containment functions. Identification and management of aging and degradation of concrete structures is fundamental to the proposed long-term operation of NPPs. Replacement of concrete structures is impractical; therefore, it is necessary that any safety issues related to plant aging and the acceptability of concrete structures for supporting long-term plant operations are resolved using sound scientific and

---

FIGURE 1. Illustrations of (a) Nuclear Power Plant (NPP) large concrete structures [1] and (b) the complexity of geothermal enhanced systems [2].

engineering understanding. Unlike most metallic materials, reinforced concrete is an heterogenous material, a composite with a low-density matrix, a mixture of cement, sand, aggregate and water, and a high-density reinforcement (typically 5% in NPP containment structures), made up of steel rebar or tendons. Concrete structures in NPPs have typically been built with local cement and aggregate fulfilling the design specification regarding material strength, workability and durability; therefore, each plant's concrete composition is unique and complex. In addition, concrete structures in NPPs are often inaccessible and contain large volumes of massively thick concrete.

Similarly, production wells in Engineered Geothermal Systems (EGS), see Fig. 1b [2], are large complex structures typically composed of layers of steel, cement, soil, and rock. The oil industry, which has been using sonic logging since 1935 [3], began developing downhole acoustic imaging capabilities in earnest since first introduced in 1970 [4]. Since that time, several companies have developed and manufactured sonic tools for inspection such as GE Sondex and Schlumberger. These currently available tools concentrate on measuring anomalies in the steel well casing and the integrity of the steel-to-grout bond. Farther penetration into the surrounding rock formation is not done [5, 6]. The industry is in need of near-wellbore in-situ characterization capabilities that will significantly improve wellbore integrity evaluation and near-wellbore fracture network mapping. A more detailed image of the fracture network near the wellbore in particular will enable the selection of optimal locations for stimulation along the wellbore, provide critical data that can be used to improve stimulation design, and provide a means for measuring evolution of the fracture network to support long-term management of reservoir operations. Note that NDE challenges for EGS are present in other well-based industries, such as carbon sequestration and the oil and gas industries.

While acoustic imaging using the synthetic aperture focusing technique (SAFT) works adequately well for thin specimens of concrete or for steel inspection, enhancements are needed for heavily reinforced, thick concrete and for near-wellbore fracture network mapping. We pursue a unique approach in order to suppress noise from ultrasound echoes and extend the imaging capabilities of borehole imaging and evaluation methods. In particular, we intend to research and develop the use of ultrasound phased arrays and model-based iterative reconstruction (MBIR) techniques. Although MBIR has been a success in the field of X-Ray CT imaging, this technique has not been ported to the field of ultrasound tomography yet. In contrast to delay-and-sum approaches like SAFT, where reconstructed pixel intensities are an integration of signal amplitudes under poor wave propagation assumptions (i.e., constant acoustic speed), our end goal is to include in MBIR comprehensive models for the acoustic system and media (e.g., approximations of wave propagation models for longitudinal and shear waves that include changes in acoustic speed throughout the media). In addition, MBIR will iterate until it finds the intensity reflectivity coefficients distribution over the field of view that best fits the data. Our end-goal is to contribute with a reconstruction method that increases the depth range of current ultrasonic probes and image quality, and provides quantitative measurements of the physical properties of the medium under interrogation. For this initial implementation, we define a forward model for acoustic p-wave propagation from an ultrasonic phased array with the following assumptions: the media is homogenous, and the Born

approximation and coherent integration hold. The paper includes a detailed description of the forward, inverted, and discretized models. Finally, we offer a toy reconstruction sample with synthetic data.

MODEL-BASED ITERATIVE RECONSTRUCTION

Model-Based Iterative Reconstruction (MBIR) is an image reconstruction framework that embraces the integrated imaging philosophy, where the hardware and software are tailored to provide the most informative measurement. It is a powerful probabilistic tool that has been proven to be very effective for reconstruction in many applications.The method has been extensively applied to the reconstruction of X-ray Computed Tomography (CT) with a superior image quality than state-of-the-art filter back projection techniques. MBIR shows equivalent image quality even after X-ray dose reductions of up to 80%. This reduction in X-ray dose is a testament of the robustness of the system in the presence of noise and sparse information collection, which are usually the interrogation conditions for thick concrete.

MBIR models the system and reconstructs the solution using the inverse problem method. MBIR works by designing a probabilistic model for the measurements (forward model) and a probabilistic model for the object (prior model). Both models are used to formulate an objective function (cost function), such as the maximum a posteriori (MAP) cost function. A typical MBIR problem revolves around finding

$$\tilde{x} = \underset{x}{\operatorname{argmin}}\{f(x)\} = \underset{x}{\operatorname{argmin}}\{-\log p(y|x) - \log p(x)\} \,,$$

where x is the unknown that we would like to estimate, $f(x)$ is the cost function, y is the measured data, $\tilde{x}$ is the estimate of x, $p(y|x)$ is the forward model, and $p(x)$ is the prior model [7]. The final step in MBIR is to optimize the cost function. While more accurate models produce high quality solutions, they make the cost function more complicated. This in return makes solving the inverse problem very computationally expensive. Therefore, many iterative reconstruction algorithms have been adopted to speed up the computation, such as Gradient Descent (GD), Conjugate Gradient (CG), Iterative Coordinate Descent (ICD), etc.

There are many iterative reconstruction methods, such as iterative maximum likelihood estimation (MLE) [8], and simultaneous iterative reconstruction technique (SIRT) [9]. The main difference between MBIR and MLE is that MLE does not require a prior model of the object, which can be sensitive to random variation in data. The prior model is necessary to regulate the estimation and reduce variance. However, this will require having an accurate prior model. Similarly, SIRT does not require a prior model, either, and does not require a probabilistic model for the measurements [10].

MBIR has been used in many tomographic applications. It has been used in X-Ray computed tomography (CT) [11], positron emission tomography (PET) [12], electron tomography [13], etc. However, MBIR has not been applied to ultrasound tomography yet. There are a few iterative non-MBIR reconstruction methods for ultrasound, such as the Born Iterative Method (BIM), which is combined with Total Variation (TV) minimization to reconstruct ultrasound computed tomography (UCT) using compressed sensing (CS) [14], and the Iterative Inverse Nonuniform Fast Fourier Transform (NUFFT), which is used in diffraction UCT [15]. While these methods can produce good results, they are intended for transmission measurements. In this paper, we show an MBIR implementation for one-sided ultrasound applications.

Our First MBIR Forward and Prior Models

To apply MBIR to the ultrasonic signals, we need to formulate the forward model $p_{y|x}(y|x)$ and the prior model $p(x)$, where y is the observed data and x is the unknown Intensity Reflectivity Coefficients (IRC).

The forward model $-\log(p_{y|x}(y|x))$ is approximated by

$$\frac{1}{2}(y - Ax)^T \Lambda (y - Ax) \,,$$

where Λ is an diagonal matrix with statistical weights and A is the system matrix defined below.

In order to compute the system matrix A, we will consider an ultrasound system that probes a position $p \in \mathbb{R}^3$ in a homogeneous medium [16] by transmitting a signal from the ith transducer located at position $r_i \in \mathbb{R}^3$ and receives the reflected signal at the jth transducer located at position $r_j \in \mathbb{R}^3$.

If the medium is linear, homogeneous, and isotropic, then the transfer function from the transmitter to the point p is given by

$$G(r_i, p, f) = \tau_1 \tau_2 \exp\{-(\alpha(f) + j\beta(f))\|p - r_i\|\}$$

where

$$\alpha(f) \approx \alpha_0|f|$$

is the rate of attenuation in $\frac{Nepers}{m \cdot Hz}$,

$$\beta(f)) \approx \frac{2\pi f}{c}$$

is the phase delay due to propagation through the medium [17]. Similarly, the transfer function from the point p to the receiver is given by

$$G(p, r_j, f) = \tau_1 \tau_2 \exp\left\{-(\alpha(f) + j\beta(f))\|p - r_j\|\right\} .$$

Let $s(t)$ be the transmitted signal, and let $x(p)$ be the IRC of the voxel at location p that we would like to measure. Then, the received signal due to reflections from the voxel $x(p)$ at location p is given by

$$
\begin{aligned}
Y_{i,j}(p, f) &= S(f)G(r_i, p, f)x(p)G(p, r_j, f) & (1)\\
&= \tau_1^2 \tau_2^2 x(p) S(f) \exp\left\{-(\alpha_0 c|f| + j2\pi f) T_{i,j}(p)\right\} & (2)
\end{aligned}
$$

where $S(f)$ is the Fourier transform of $s(t)$, and

$$T_{i,j}(p) = \frac{\|p - r_i\| + \|p - r_j\|}{c} . \qquad (3)$$

From Eq. 1, the system point spread function (PSF) is defined as

$$h(T_{i,j}(p), t) = \mathcal{F}^{-1}\left\{\tau_1^2 \tau_2^2 S(f) \exp\left\{-\alpha_0 c|f|T_{i,j}(p)\right\}\right\} \qquad (4)$$

Then, the received signal amplitude at time t is given by

$$y_{i,j}(p, t) = h(T_{i,j}(p), t - T_{i,j}(p)) x(p) \qquad (5)$$

Finally, the full signal transmitted and received by transducer i and j, respectively is computed by integrating over p.

$$y_{i,j}(t) = \int_{\mathbb{R}^3} y_{i,j}(p, t)dp = \int_{\mathbb{R}^3} A_{i,j}(T_{i,j}(p), t)x(p)dp , \qquad (6)$$

where the system matrix is defined as

$$A_{i,j}(T_{i,j}(p), t) = h(T_{i,j}(p), t - T_{i,j}(p)). \qquad (7)$$

Fig. 2 illustrates the system matrix A coefficients for the row corresponding a time of $133\mu s$. The forward model was generated for a single transducer pair located at the bottom-left and top-left of the propagation plane. The input signal $s(t)$ is a five-cycle sine wave tapered with a Hanning Window. As expected, the coefficients' amplitudes are constant at equal propagation distances. Similarly, the coefficients at system matrix rows corresponding to a longer propagation time are smaller due to attenuation.

The prior model is assumed a q-Generalized Gaussian Markov Random Fields (q-GGMRF) [18], which is defined as

$$U(x) = -\log(\boldsymbol{p}(x)) \approx \frac{1}{v\sigma^v} \sum_{j,k \in C} b_{i,k} \, \rho(x_i - x_k) \text{ and } \rho(\Delta) = \frac{|\Delta|^u}{1 + |\Delta/50|^{u-v}}$$

where σ is a scalar determined empirically and controls the prior influence on the solution, C is the set of pixels in the neighborhood of x, and $1 \le u \le v \le 2$.

Discretization

The Quadrature Method [19] was employed for discretization of the forward model. If we observe until $t = T$, where T is the maximum expected roundtrip time for the ultrasonic signal, then, there is no need to integrate over $\mathbb{R}^3$. It suffices to integrate over a region where sound reaches $\frac{T}{2}$ seconds. This makes

$$p \in \Omega = \left\{ \begin{bmatrix} p_1 \\ p_2 \\ p_3 \end{bmatrix} ; 0 \le p_1 \le M_1, -M_2 \le p_2 \le M_2, -M_3 \le p_3 \le M_3 \right\}$$

where M_1, M_2, and M_3 are chosen in a way to ensure all points outside Ω are neglected in the integral of Eq. 6. Let Δ_1, Δ_2, and Δ_3 be the distance between each pixel along the three dimensional axes. Let

$$m_1 = \frac{M_1}{\Delta_1}, \; m_2 = \frac{M_2}{\Delta_2}, \; m_3 = \frac{M_3}{\Delta_3}.$$

Consequently, we can discretize the system matrix and object to reconstruct by

$$A_{i,j}[k_1, k_2, k_3, n] = \Delta_1 \Delta_2 \Delta_3 A_{i,j}(\Delta_1 k_1, \Delta_2 k_2, \Delta_3 k_3, T_0 n) \tag{8}$$
$$x[k_1, k_2, k_3] = x(\Delta_1 k_1, \Delta_2 k_2, \Delta_3 k_3), \tag{9}$$

then

$$
\begin{aligned}
y_{i,j}[n] &= y_{i,j}(T_0 n) \\
&\approx \Delta_x \Delta_y \Delta_z \sum_{k_3=-m_3}^{m_3} \sum_{k_2=-m_2}^{m_2} \sum_{k_1=1}^{m_1} A_{i,j}(\Delta_1 k_1, \Delta_2 k_2, \Delta_3 k_3, T_0 n) x(\Delta_1 k_1, \Delta_2 k_2, \Delta_3 k_3) \\
&= \sum_{k_3=-m_3}^{m_3} \sum_{k_2=-m_2}^{m_2} \sum_{k_1=1}^{m_1} A_{i,j}[k_1, k_2, k_3, n] x[k_1, k_2, k_3]
\end{aligned}
$$

where T_0 is the time sampling rate. The same approach was employed to discretize the prior model $U(p)$ to $U[k_1, k_2, k_3]$.

This permits the construction of the forward model for each transducer pair $< i, j >$ as

$$Y_{i,j} = A_{i,j} X,$$
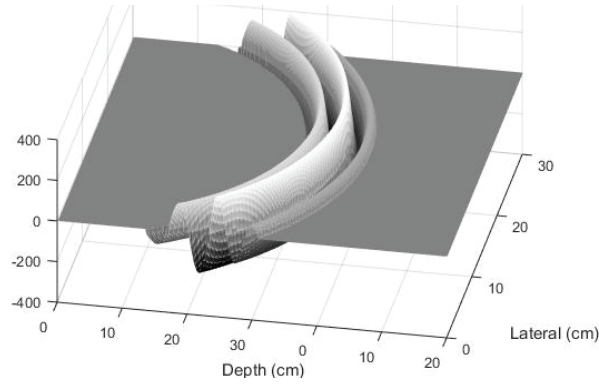
FIGURE 2. Illustration of system matrix coefficient amplitudes for two transducers at time $133 \mu s$.

where

$$Y_{i,j} = \begin{bmatrix} r_{i,j}[1] \\ r_{i,j}[2] \\ \vdots \\ r_{i,j}[N-1] \\ r_{i,j}[N] \end{bmatrix}_{N \times 1}$$

$$X = \begin{bmatrix} X[1, -m_2, -m_3] \\ X[2, -m_2, -m_3] \\ \vdots \\ X[m_1, -m_2, -m_3] \\ X[1, 1-m_2, -m_3] \\ \vdots \\ X[m_1, m_2, -m_3] \\ X[1, -m_2, 1-m_3] \\ \vdots \\ X[m_1, m_2, m_3] \end{bmatrix}_{(m_1(2m_2+1)(2m_3+1)) \times 1}$$

and,

$$A_{i,j} = \begin{bmatrix} A_{i,j}[1, -m_2, -m_3, 1] & \dots & A_{i,j}[m_1, -m_2, -m_3, 1] & \dots & A_{i,j}[m_1, m_2, m_3, 1] \\ A_{i,j}[1, -m_2, -m_3, 2] & \dots & A_{i,j}[m_1, -m_2, -m_3, 2] & \dots & A_{i,j}[m_1, m_2, m_3, 2] \\ & & \vdots & & \\ A_{i,j}[1, -m_2, -m_3, N] & \dots & A_{i,j}[m_1, -m_2, -m_3, N] & \dots & A_{i,j}[m_1, m_2, m_3, N] \end{bmatrix}_{N \times (m_1(2m_2+1)(2m_3+1))} . \quad (10)$$

Note that multiple transducers pairs can be added to the MBIR forward model by concatenating their corresponding forward models and measurements to A and Y, respectively. The number of pairs is limited by the amount of computational memory available. However, our initial assessment of the system matrix indicates that the matrix is sparse. There are methods for sparse large matrices that permit to process such matrices under constrained computational resources [20]. Consequently, we do not foresee computational memory to be a limiting factor when designing our ultrasonic phased array. Finally, we can define our optimization function as

$$\tilde{x} = \underset{x}{\operatorname{argmin}} \{ \frac{1}{2}(Y - AX)^T \Lambda (Y - AX) + U \}.$$

SYNTHETIC RESULTS

The initial forward model was tested with synthetic data. This test was performed to confirm the correctness of the propagation model and to have a better insight on the influence of the q-GGMRF prior model on the solution. For the initial test, we assumed an homogenous cement slab with acoustic speed of $3,680\,m/s$ and attenuation coefficient of $4.8 \times 10^{-5} \frac{Nepers}{m \cdot Hz}$. The ultrasound system is defined as non-focused isotropic sources and sensors, where the input signal is a single-cycle sine wave with a central frequency of $100KHz$ and a bandwidth of $150KHz$. Consequently, the expected axial resolution is approximately $2cm$. Two phantom test samples were generated for the synthetic test (See Fig. 3). The positive pixel intensities in the phantom images correspond to the IRC values for changes in impedance (i.e., interfaces where the current material ends and a new material starts, for example, the cement to steel interface with an IRC of 0.525). Fig. 3a shows a one-dimensional object with two interfaces at $35cm$ and $65cm$ deep with IRC amplitudes of 0.525 and 0.95, respectively. For this phantom, transmission and receiving are performed by the same transducer positioned at the origin (i.e., $0cm$). Fig. 3b illustrates a two-dimensional phantom sample with two impedance changes at $18cm$ and $35cm$ deep with IRC amplitudes of 0.525 and 0.95, respectively. Ten transducers
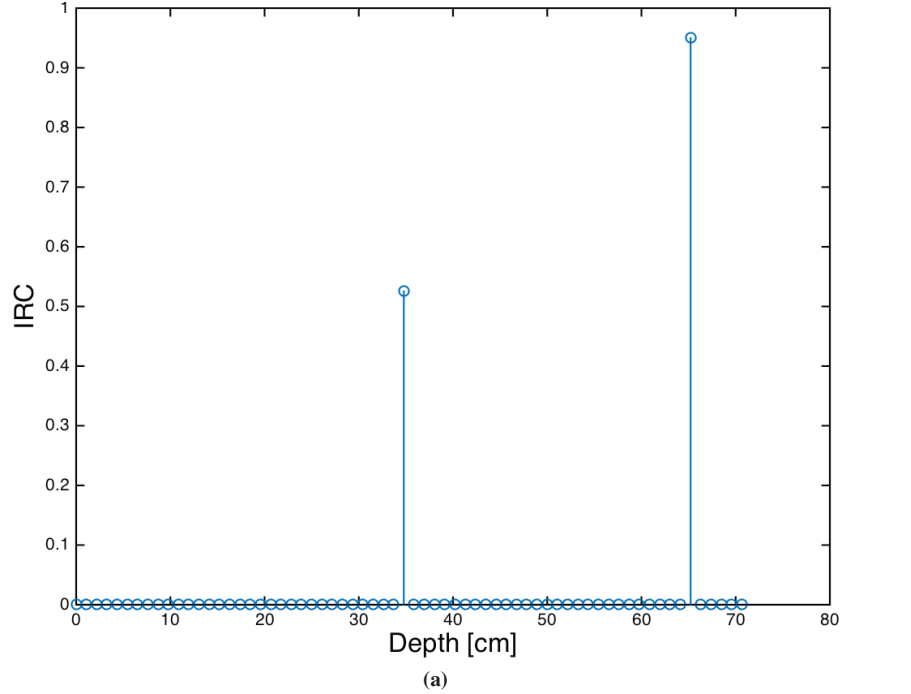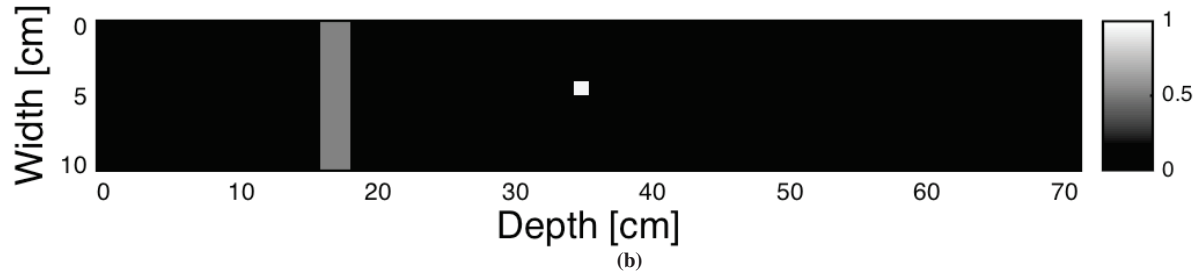
FIGURE 3. Phantom samples used for the synthetic test. (a) One-dimensional object with two impedance changes interfaces. (b) Two-dimensional object with two embedded interfaces of different widths and lengths.

were placed at the origin–one at each row. Note that the first interface extends the full width of the medium and the second interface is a small, highly reflective impurity.

The synthetic signal was generated using conventional sound propagation models. Diffraction and mode-conversion (i.e., p-wave to s-wave conversion) were not included in the current simulation. We added Gaussian noise to the synthetic signal to emulate electrical noise in the components of the ultrasound system. Fig. 4a shows a plot of the synthetic signal generated from the phantom in Fig. 3a. We selected Iterative Coordinate Descent (ICD) as the optimization algorithm [18], which shows fast and stable convergence. Usually, the algorithm is initialized with a low frequency (i.e., blurred) version of the object. The low frequency initial object estimate could be obtained from back projection $\tilde{x}_0 = A^T Y$ or from other reconstruction techniques such as SAFT. Initializing the object with a quick low frequency estimate is the ideal reconstruction workflow given that ICD emphasizes high frequency components during convergence. For the one-dimensional case, in Fig. 4b, the reconstruction algorithm obtained IRC values of 0.536 and 0.953 for the first and second interfaces, respectively. We stopped the ICD algorithm after 500 iterations. For the two-dimensional case, in Fig. 4c, the estimated interface IRC coefficients converged to 0.524 and 0.878 after 5000 iterations. Although these initial results are very encouraging, we can further improve the accuracy of our reconstructions by adjusting our prior model regularization parameters.
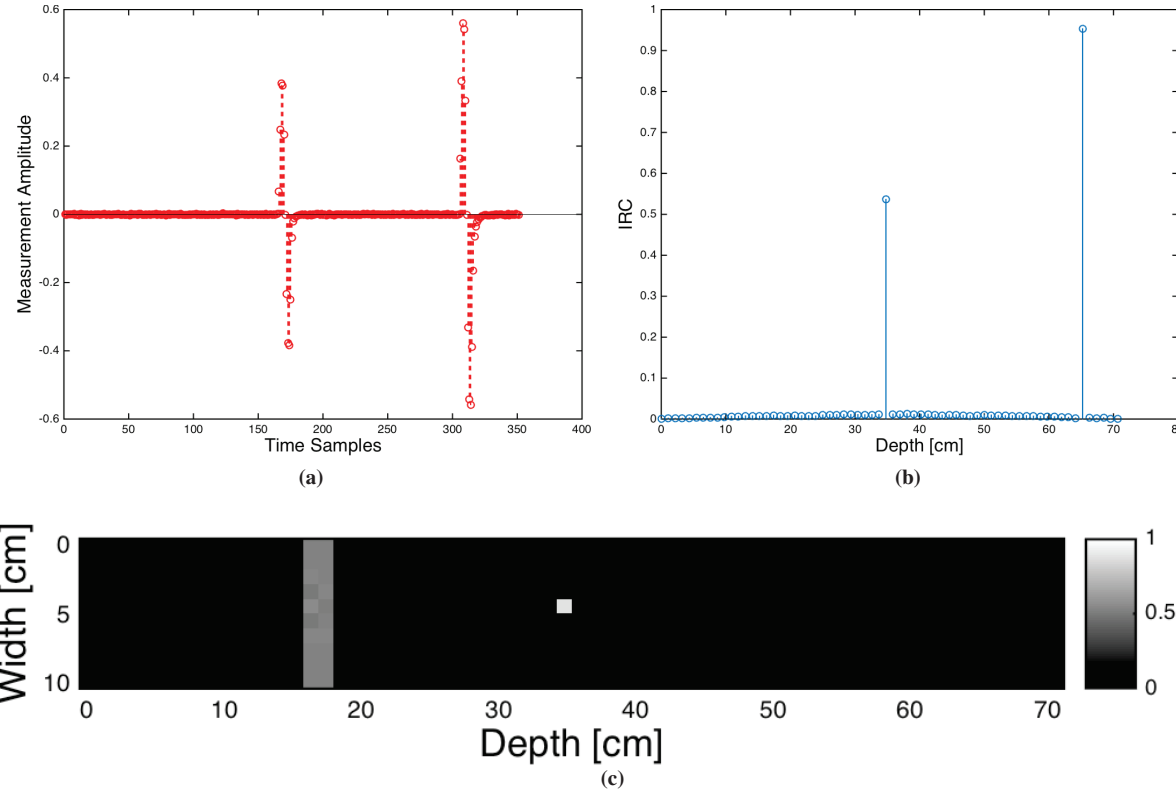
FIGURE 4. (a) Synthetic measured reflections for the phantom in Fig. 3a, and reconstruction results for the (b) one-dimensional and (c) two-dimensional phantoms.

CONCLUSION

We have developed an initial implementation of the MBIR algorithm for ultrasonic signals. The current algorithm assumes isotropic sources and sensors with longitudinal waves (i.e., p-waves) propagating in an homogenous medium. In contrast to delay and sum approaches as SAFT, our approach reconstructs actual IRC values as shown in the synthetic experiments. There are a few features that we need to incorporate to our current forward model in order to successfully reconstruct real data. For example, actual transmitters are not isotropic; the input signal strength typically decreases for the sound vectors away from the transducer optical axis. Our end-goal is to reconstruct complex and heterogeneous solid objects. Consequently, future implementations of the forward model most include diffraction and conversion-mode models. Our biggest challenge is to incorporate these complex features while keeping the forward model tractable and computational efficient.

ACKNOWLEDGMENTS

REFERENCES

1   Wikimedia Commons, Chapelcross Nuclear Power Station, https://upload.wikimedia.org/wikipedia/commo ns/7/7e/Chapelcross_Nuclear_Power_Station_2.jpg (October 2006).

2   Wikimedia Commons, EGS Diagram, https://upload.wikimedia.org/wikipedia/commons/thumb/c/c6/ EGS_diagram.svg/500px-EGS_diagram.svg.png (October 2009), Siemens Press.

3   C. Schlumberger, Method of and Apparatus for Surveying the Formations Traversed by a Bore Hole, https://www.google.com/patents/US2191119 (1940), U.S. Patent, Patent #2,191,119.

4   J. Zemanek, E. E. Glenn, L. J. Norton, and R. L. Caldwell, Geophysics **35**, 254–269 (1970).

5   J. Arroyo-Franco, M. Mercado-Oritz, L. R. G. De, and S. Williams, Oilfield Review **18**, 14–33 (2006).

6   J. Haldorsen, D. Johnson, T. Plona, B. Sinha, H. Valero, and K. Winkler, Oilfield Review **18**, 34–43 (2006).

7   C. Bouman, *Model Based Image Processing*, 1st ed. (Purdue University, 2013) https://engineering.purdue.edu/ bouman/publications/pdf/MBIP-book.pdf.

8   Q. Wang and G. Ren, IEEE Transactions on Wireless Communications **14**, 2778–2787May (2015).

9   Z. Haiyan, S. Xiuli, Q. Xuerui, F. Shixuan, L. Xiao, and L. Donghui, "Lamb wave tomography combining simulated annealing and simultaneous iterative reconstruction technique," in *Microwave Conference* (2008), pp. 741–744.

10 S. Venkatakrishnan, L. Drummy, M. Jackson, M. D. Graef, J. Simmons, and C. Bouman, IEEE Transactions on Image Processing **22**, 4532–4544November (2013).

11 Z. Yu, J. Thibault, C. Bouman, K. Sauer, and J. Hsieh, IEEE Transactions on Image Processing **20**, 161–175January (2011).

12 M. E. Kamasak, C. A. Bouman, E. D. Morris, and K. Sauer, IEEE Transactions on Medical Imaging **24**, 636–650May (2005).

13 Z. H. Levine, A. J. Kearsley, and J. G. Hagedorn, J. Res. Nat. Inst. Stand. Technol **11**, 411–417Nov (2006).

14 R. V. Sloun, A. Pandharipande, M. Mischi, and L. Demi, IEEE Transactions on Biomedical Engineering **62**, 1660–1664June (2015).

15 J. A. Fessler, "Iterative tomographic image reconstruction using nonuniform fast fourier transforms," Technical Report (Communications and Signal Processing Laboratory Department of Electrical Engineering Computer Science, University of Michigan, 2001).

16 S. J. Norton and M. Linzer, IEEE Transactions on Biomedical Engineering **BME-28**, 202–220February (1981).

17 A. Kak and K. A. Dines, IEEE Transactions on Biomedical Engineering **BME-25**, 321–344July (1978).

18 J.-B. Thibault, K. Sauer, C. Bouman, and J. Hsieh, Medical Physics **34**, 4526–4544November (2007).

19 L. Soldo and N. Wider, Discretization of Linear Inverse Problems, https://www.math.ethz.ch/education/bachelor/seminars/hs2010/ipip/slides.6.pdf (2011).

20 N. Bell and M. Garland, "Implementing Sparse Matrix-vector Multiplication on Throughput-oriented Processors," in *Proceedings of the Conference on High Performance Computing Networking Storage and Analysis*, 18 (ACM, 2009), pp. 18:1–18:11.